Frictional behavior of input sediments to the Hikurangi Trench, New Zealand

H.S. Rabinowitz[1], H.M. Savage[2,3], R.M. Skarbek[2], M.J. Ikari[4], B.M. Carpenter[5], C. Collettini[6]

[1] Brown University, Providence, RI.
[2] Lamont-Doherty Earth Observatory, Palisades, NY.
[3] Department of Earth and Environmental Science, Columbia University, New York, NY.
[4] University of Bremen, Bremen, Germany.
[5] University of Oklahoma, Norman, OK.
[6] Dipartimento di Scienze della Terra, Sapienza Università di Roma, Rome, Italy.

Corresponding author: Hannah Rabinowitz (hannah_rabinowitz@brown.edu)

Key Points:

- Sediments subducting at the Hikurangi Trench become weaker and less velocity-strengthening with increasing depth.
- Sediments exhibit a cut-off velocity of 1μm/s, possibly explaining the presence of shallow slow slip at the Hikurangi Trench.
- Slow slip at the Hikurangi Trench could result from frictional instability, in addition to factors such as elevated pore fluid pressures.

This article has been accepted for publication and undergone full peer review but has not been through the copyediting, typesetting, pagination and proofreading process which may lead to differences between this version and the Version of Record. Please cite this article as doi: 10.1029/2018GC007633

Abstract

The Hikurangi subduction zone hosts shallow slow slip events, possibly extending to the seafloor. The mechanisms allowing for this behavior are poorly understood, but are likely a function of the frictional properties of the down-going seafloor sediments. We conducted friction experiments at a large range of effective stresses, temperatures, and velocities on incoming sediment to the Hikurangi subduction zone to explore the possible connection of frictional properties to slow slip events (SSEs). These experiments were conducted on multiple apparatuses, allowing us to access a wider range of deformation conditions than is available on any one machine. We find that the material frictionally weakens and becomes less velocity strengthening with increasing effective stress, whereas temperature has only a small effect on both friction and frictional stability. When driven at the plate-convergence rate, the sediment exhibits velocity-weakening behavior. These results imply that the frictional properties of the sediment package subducting at Hikurangi could promote slow slip events at the pressures, temperatures, and strain rates expected along the plate boundary thrust up to 10 km depth without requiring elevated pore fluid pressures. The transition to velocity strengthening behavior at faster slip rates could provide a mechanism for limiting unstable slip to slow sliding velocities, rather than accommodating deformation through ordinary earthquakes.

1. Introduction

Strain at plate boundaries is accommodated over a wide range of deformation rates, ranging from earthquake slip to aseismic creep. Within this spectrum are slow slip events (SSEs), which last for days to months (Dragert et al., 2001, 2004; Ide et al., 2007; Obara, 2002; Ozawa et al., 2007; Vallée et al., 2013; Wallace and Beavan, 2010). SSEs at the Hikurangi Trench are observed at a wide range of depths (Wallace et al., 2012; Wallace and Beavan, 2010, 2006), and may play an important role in loading seismogenic fault segments (Hamling and Wallace, 2015; Ito et al., 2013; Kato et al., 2012). Along the Hikurangi subduction zone of the North Island of New Zealand, shallow SSEs extend to depths <2 km (Wallace et al., 2016) and show a complex relationship with regional deformation, by triggering microseismicity on the subducting slab interface (Delahaye et al., 2009) and being triggered by nearby earthquakes (Wallace et al., 2017). In addition, the region in which shallow SSEs occur has hosted historical tsunami earthquakes, which are characterized by anomalously long source durations, slightly slower rupture velocities, and a large amount of low-frequency energy relative to their moment (Pelayo and Wiens, 1992; Doser and Webb, 2003; Bell et al., 2014). These interactions between slow slip and damaging tectonic earthquakes highlight the importance of investigating the mechanisms that control SSEs.

Previous work has suggested that shallow slow slip at Hikurangi (<15 km depth) and other subduction zones is a condition of frictional stability, which can be modulated by effective stresses, material properties of the fault rocks, or a combination of these factors (Saffer and Wallace, 2015). Changes in frictional stability can be promoted by elevated pore fluid pressures through a reduction in effective stress, as has been proposed at Hikurangi (Bassett et al., 2014; Bell et al., 2010; Ellis et al., 2015). In addition, slow slip could be facilitated by a transition from frictionally stable to frictionally unstable or conditionally stable behavior through a reduction in the friction rate parameter, $a–b$, which indicates

whether a material will frictionally weaken or strengthen with a change in slip velocity (described in Section 2.3; Dieterich, 1979, Ruina, 1983). The shallow parts of subduction zones tend to be dominated by clays, which often exhibit frictionally stable behavior and are frequently invoked as the cause of the up-dip limit of the seismogenic zone where earthquakes nucleate (Hyndman et al., 1997; Moore and Saffer, 2001; Scholz, 1998). One important consideration is that subducting sediments often include multiple lithologies, which can impact frictional transitions along the slab interface. Sediments with a range of compositions (including clays and carbonates) can become more frictionally unstable at pressure and temperature conditions relevant to shallow subduction zone environments (den Hartog et al., 2012a, 2012b; Ikari et al., 2013b; Kurzawski et al., 2016), possibly allowing the nucleation of quasi-unstable slip such as SSEs. It is important to characterize the frictional behavior of sediments subducting at individual subduction zones in order to assess the role that pressure, temperature, sliding velocity and composition have in controlling the occurrence of SSEs.

In this work, we investigate the frictional behavior of sediment on the incoming plate of the Hikurangi Trench (ODP Site 1124; Figure 1a,b) (Plank, 2014). The upper portion of the incoming stratigraphy consists of a mixture of carbonate and clay (Figure 1b), and is likely similar to the material within the shallow subduction zone. Through velocity-stepping friction experiments at a range of effective stresses and temperatures, as well as new plate-rate experiments (Ikari et al., 2015; Ikari and Kopf, 2017), we investigate the strength and stability of this mixed sedimentary material.

2. Background

2.1. Slow slip in subduction zones

Slow slip in subduction zones was first observed in Japan and Cascadia (Dragert et al., 2001; Rogers and Dragert, 2003; Sacks et al., 1978; Hirose et al., 1999) and has now been

observed in many subduction zones around the world (Ide et al., 2007; Ito et al., 2013; Ito and Obara, 2006; Kato et al., 2012; Obara, 2002; Ozawa et al., 2007; Peng and Gomberg, 2010; Vallée et al., 2013; Wallace et al., 2012; Wallace and Beavan, 2006). Slow slip can be detected geodetically, or inferred through seismically detectable events such as non-volcanic tremor (Rodgers and Dragert, 2003; Obara and Hirose, 2006; Payero et al., 2008; Walter et al., 2011). Here, we use the term slow slip to include all of these observations where a fault slips in discrete events at subseismic velocities. Slow slip is often observed at the down-dip limit of the seismogenic zone (Peng and Gomberg, 2010). It is generally interpreted as a frictionally transitional deformation behavior and is often associated with high pore fluid pressures (Audet et al., 2009; Saffer and Wallace, 2015). Although harder to detect because of observational constraints, SSEs also occur above and within the seismogenic zone (Araki et al., 2017; Outerbridge et al., 2010; Wallace et al., 2016; Wallace et al., 2012). SSEs have been observed as precursors to large megathrust earthquakes, such as the 2001 M_w8.4 Peru earthquake (Melbourne and Webb, 2002), the 2011 M_w9.0 Tohoku-oki earthquake (Ito et al., 2013; Kato et al., 2012), and the 2014 M_w7.3 Papanoa earthquake (Radiguet et al., 2016), demonstrating that they may increase stress within seismogenic zones in some cases.

2.2. Hikurangi shallow slow slip and stratigraphy of Leg 181 ODP Site 1124

The Hikurangi margin can be divided into southern and northern sections based on both geomorphic character and observed slip behavior. The convergence rate of the Australian and Pacific Plates also varies dramatically along the trench from a rate of ~2 cm/y in the south, increasing to ~6 cm/y in the north (Wallace et al., 2004). Geodetic coupling varies along the margin as well. The southern section is coupled to ~30 km depth while the northern section is coupled only to ~5–15 km depth (Wallace et al., 2004; Wallace and Beavan, 2010). The Hikurangi margin exhibits a paucity of large magnitude megathrust earthquakes. The largest recorded earthquakes at Hikurangi are two ~M_w7 events that occurred along the northern

section near Gisborne in 1947 (Bell et al., 2014; Doser and Webb, 2003), and there are no M_w>7.2 subduction interface earthquakes in the historic record (Wallace et al., 2009). Deformation along the margin seems to be largely accommodated by SSEs with an equivalent seismic moment release of ~M_w 6.5–7 (Wallace et al., 2012). These SSEs fall into two main categories. Deep SSEs occur in the southern section at depths of ~20–50 km, have durations of ~1.5 years, and repeat times of ~5 years (Wallace et al., 2012; Wallace and Beavan, 2010). Shallow SSEs in the northern section of the margin occur where a relatively thin sedimentary package (~1 km as compared to ~3–6 km in the south) is subducting (Davy and Wood, 1994; Lewis et al., 1998). These shallow SSEs have durations of 1–3 weeks, recur approximately every 1–2 years and may propagate to the trench (Beavan et al., 2007; Douglas et al., 2005; Wallace et al., 2016, 2012; Wallace and Beavan, 2010). These events appear to be correlated with zones of elevated pore fluid pressure within fault rocks characterized by transitional frictional behavior (Bell et al., 2010; Ellis et al., 2015; Saffer and Wallace, 2015).

Another important factor to constrain in order to understand slow slip is the frictional behavior of the sediments subducting at the Hikurangi Trench. Extensive work on subduction zone sediments has highlighted the evolution of frictional behavior at a continuum of slip rates (Buijze et al., 2017; Faulkner et al., 2011; Ikari et al., 2013a, 2011a; Ikari and Kopf, 2017; Ujiie et al., 2013; Vannucchi et al., 2017). At a distance of ~500 km, ODP Site 1124 is the closest existing ocean drill core through the input sediments to the Hikurangi Trench (Figure 1a). Core recovered at this site extends to a depth of ~470 mbsf and is composed primarily of nanofossil ooze interlayered with clays and mudstones (Carter et al., 2000). In this study, we investigate the frictional behavior of carbonate-rich sediment sampled from cores at Site 1124 (Figure 1b).

2.3. Friction of subducting sediments

Because clays are common in subducting sediments and fault gouges (Underwood, 2002, 2007), there has been considerable effort towards characterizing clay friction. Studies consistently show that clays are weaker than most other materials, exhibiting friction (μ) values significantly below Byerlee friction (μ = 0.6) in both dry and wet experiments (Bird, 1984; Byerlee, 1978; Faulkner et al., 2011; Ikari et al., 2009b; Moore and Lockner, 2007; Morrow et al., 1992a; Saffer et al., 2012, 2001; Saffer and Marone, 2003; Tembe et al., 2010). Unlike many other materials, which maintain a pressure dependent shear strength (constant friction coefficient) through upper crustal conditions, some clays exhibit a rapid reduction in friction at relatively low effective stresses of ~30 MPa, indicating a rollover in the Mohr-Coulomb failure envelope as the material transitions to pressure independent shear strength with increasing effective stress (Bird, 1984; Saffer et al., 2001; Saffer and Marone, 2003).

Clays not only control the steady-state friction of a fault zone, but may also control the fault stability. Frictional stability can be described using a rate-and-state friction framework, where friction is a function of both sliding velocity and time. With a step in velocity, there is an immediate change in friction described as the direct effect, a, followed by the evolution of μ to a new steady-state value, known as the evolution effect, b. Materials are considered velocity-strengthening, or frictionally stable, if $a–b>0$ and velocity-weakening if $a–b<0$ (Marone, 1998). When a material is velocity-weakening and its surroundings are sufficiently compliant, it is considered frictionally unstable (Scholz, 1998; Tullis and Weeks, 1986). Clays are largely velocity-strengthening, though at low effective stresses and low sliding velocities they can be velocity-weakening (Ikari et al., 2013b; Saffer et al., 2001; Saffer and Marone, 2003; Ikari and Kopf, 2017).

While the behavior of clay-rich material at a range of effective stress conditions relevant to shallow subduction zones is well established, fewer studies have focused on the effects of

temperature on clay friction. For example, talc strength decreases with increasing temperature and exhibits only velocity strengthening behavior over a range of ~100–400 ˚C (Moore and Lockner, 2008; Tembe et al., 2009). Deformation experiments on illite at a range of temperatures have shown an increase in frictional strength with increasing temperature, and the occurrence of velocity-weakening behavior and unstable stick-slip at temperatures above 200 ˚C (den Hartog et al., 2012a, 2012b, Moore et al., 1989, 1986, 1983). Additionally, experiments on natural fault materials show that gouges with significant amounts of smectite exhibit increasing friction with increasing temperature as well as a reduction in $a–b$ at elevated temperatures (Niemeijer et al., 2016; Tembe et al., 2009). Another important consideration is the effect of sliding velocity on frictional stability. Slow slip can be promoted over conventional earthquake slip by an increase in $a–b$ (indicating a transition towards frictional stability) with increasing sliding velocity. This transition from negative to positive values of $a–b$ as a function of sliding velocity is known as the cutoff velocity (Shibazaki and Iio, 2003; Shibazaki and Shimamoto, 2007). Recent room temperature plate-rate experiments show that gouge with high clay contents from a range of plate boundary faults exhibits velocity-weakening behavior and slow slip instabilities when deformed at sliding velocities of 5–25 cm/yr, similar to tectonic plate rates (Ikari et al., 2015; Ikari and Kopf, 2017).

Although phyllosilicates tend to lower the frictional strength of materials, even when these weak phases do not constitute a large fraction of the bulk volume of the material (Giorgetti et al., 2015; Ikari et al., 2007; Moore and Lockner, 2011; Niemeijer et al., 2010; Saffer and Marone, 2003; Tembe et al., 2010), calcite is the largest mineral component of the sediment in our Hikurangi sample (Figure 1b) and has distinct frictional properties. Experiments on pure calcite and calcite-rich sediment from the Middle America Trench offshore Costa Rica show that carbonate-rich sediment exhibits unstable, stick-slip, velocity-

weakening behavior at a range of pressures and temperatures relevant to shallow subduction zone environments (Ikari et al., 2013b; Kurzawski et al., 2016; Verberne et al., 2014a, 2014b, 2013; Vannucchi et al., 2017). Because of this velocity-weakening frictional behavior, the presence of calcite in a subducting sediment package could imply the potential for seismogenic conditions at shallow depths.

3. Methods

Friction experiments were conducted on calcareous mudstone input sediment from ODP Site 1124C (Figure 1a, Cores 181-1124C-20X-5W, 0–18 cm; 181-1124C-21X-5W, 0–18 cm; and 181-1124C-22X-5W, 0–18 cm). Sediment from the cores was crushed with a mortar and pestle and sieved to a grain size of <125 μm in order to homogenize the experimental gouge. The composition of our sample was quantified by X-Ray Diffraction (XRD), including clay mineral species (see Vogt et al., 2002). The X-ray diffractograms were measured on a fine powder (< 20μm particle size) in a Philips X'Pert Pro multipurpose diffractometer equipped with a Cu-tube (k_α 1.541, 45 kV, 40 mA), a fixed divergence slit of ¼°, a secondary Ni filter and an X'Celerator detector system. We use a double identification method, which minimizes potential problems with overlapping peaks. The first mineral identification was done using Philips software X'Pert HighScore™ and with the X-ray diffraction interpretation software MacDiff 4.25 (e.g. Petschick et al., 1996). Specific mineral species, including individual clays and serpentine, were then identified from a database of about 300 different phase reference minerals in the QUAX database (Vogt et al., 2002). By using the extensive QUAX database and a full-pattern, multiple X-ray peak mineral identification on bulk powder, separation and treatment of the clay-sized (< 2 μm) fraction is not necessary.

Based on this measurement, our sample is composed of 43 wt% calcite, 20 wt% phyllosilicates, 15 wt% feldspar, and 9 wt% quartz (Figure 1b). Experiments were conducted

using mock brine approximating the composition of seawater, made by combining 35 g of sea salt with 1 L of distilled water. Using a pore fluid composition that reflects natural compositions is essential because pore fluid composition can affect the deformation behavior of gouge. This is particularly true for calcite-rich gouge which has been shown to exhibit higher rates of pressure solution when deformed with NaCl brine compared with pure water (Zhang and Spiers, 2005). We note that for experiments conducted on BRAVA and in direct shear, gouge layers were constituted with this brine while for experiments conducted in the triaxial deformation apparatus, gouge layers were formed by wetting the sediment with deionoized water. Mixing brine with the dried sediment (which likely has salts left behind by the *in situ* pore fluids) could yield artificially high salinity in the gouge layers composed with brine.

Friction experiments were conducted on three different deformation apparatuses to test the range of stresses, temperatures, and velocities expected along the Hikurangi subduction interface (Figure 2). By using multiple deformation apparatuses, we are able to investigate a wide range of these conditions. In addition, interlab comparisons confirm that reported friction values are consistent, and that lab variability such as jacketing and piston friction in different apparatuses is accurately accounted for. Low effective stress (σ_{eff}) experiments (σ_{eff} = 1–25 MPa) were conducted on the biaxial deformation apparatus at the Istituto Nazionale di Geofisica e Vulcanologia (INGV) in Rome while higher σ_{eff} (σ_{eff} = 25–150 MPa) and elevated temperature experiments were conducted on the triaxial deformation apparatus at the Lamont-Doherty Earth Observatory (LDEO) in New York. Further direct shear experiments (plate-rate experiments) were conducted at the University of Bremen to test the frictional behavior of the gouge at plate convergence rates of ~5.3 cm/yr (1.7 nm/s). As we discuss in the following sections, there is broad agreement in steady-state friction and *a*–*b* values

between apparatuses (Figure 3). However, there are some differences in the loading curves that relate to initial and boundary conditions (see Discussion, Figure 2).

3.1. Biaxial Deformation Experiments

Biaxial deformation experiments were conducted on the Brittle Rock deformAtion Versatile Apparatus (BRAVA) at INGV in a double-direct shear configuration (Figure 2a)(Collettini et al., 2014). Horizontal and vertical forces were measured using stainless steel load cells with ±0.03 kN resolution. Displacements were measured using LVDTs with ±0.1 μm resolution. Data was recorded at 10 kHz and down sampled to 1–1000 Hz depending on the shearing velocity. Gouge was sandwiched in two layers between three grooved forcing blocks in ~6 mm thick layers. This assembly was then jacketed in a rubber jacket to isolate the gouge from the confining fluid during the experiment. The jacketed assembly was placed in the pressure vessel and an initial normal stress of ~1 MPa was applied to hold the assembly in place and the sample was allowed to compact at this stress for 30 minutes. The vessel was then sealed and a confining pressure of ~0.5 MPa was applied by pumping silicone oil into the pressure vessel. Pore fluid pressure was then applied to ~0.25 MPa, except for sample i205 which was brought up to the experimental conditions of σ_N=0.8 MPa, P_c=0.7 MPa, and P_p=0.5 MPa. The samples were allowed to equilibrate at these conditions for another 30 minutes. Confining pressure (P_c), normal stress (σ_N), and pore fluid pressure (P_p) were then raised in parallel to the experimental values for the higher σ_{eff} experiments over the course of approximately 15 minutes. After confirming that the gouge layer was no longer compacting, the central forcing block was driven downward at a rate of 10 μm/s for a run-in of ~5 mm until maximum friction was reached. The samples exhibited significant strain weakening after the run-in phase (Figure 2d). Following the run-in phase, velocity-stepping tests were conducted at sliding velocities ranging from 1–300 μm/s to test the velocity-dependence of friction. Slide-hold-slide (SHS) tests were conducted with hold times ranging from 1–1000 s to test the healing rates of the material.

3.2. Triaxial Deformation Experiments

High pressure and temperature deformation experiments were conducted on the triaxial deformation apparatus at LDEO. These experiments were conducted using a 45˚ saw-cut configuration with 3.5 cm diameter cylindrical stainless steel forcing blocks (Figure 2c). Gouge was mixed with deionoized water to create a paste that was then spread in an even ~2.1 mm thick layer on one forcing block using a loading jig. The sample was pre-compressed between the two forcing blocks for 1 hour in a hydraulic press with an axial load of 4.5 MPa, yielding a gouge layer ~1.85 mm thick. The sample assembly was then jacketed with an inner 50 μm thick Cu foil jacket to hold the forcing blocks and gouge together throughout the rest of the loading process. This assembly was placed within a silicone rubber jacket, which extended to cover an o-ring on the top end plug as well as an o-ring on the bottom end cap. The jacket was held in place using stainless steel tourniquets wrapped tightly over these o-rings in order to create a gas-tight seal around the sample.

Pore fluid pressure was applied by pumping brine through high-pressure tubing and through the top stainless steel end plug and was distributed across the sample surface through five holes in the top forcing block. Stainless steel frits (3mm thick, 40 μm porosity) in the top forcing block prevented gouge from being extruded into the pore fluid system. A teflon shim was placed between the bottom forcing block and end cap to reduce the sliding friction between the forcing block and piston interface during deformation.

The assembly for high temperature experiments included insulating alumina end caps, which were placed between the forcing blocks and upper end plug and lower end cap. For these experiments, a coiled resistive heater was tightly wrapped around the Si rubber jacket, followed by a layer of insulation and aluminum foil. The ends of the insulation were held in place with a layer of self-fusing silicone rubber tape.

This assembly was loaded into the pressure vessel and the piston was advanced until it hit the bottom forcing block. Confining pressure and pore pressure were applied in parallel,

keeping P_c at least 5 MPa higher than P_p until the target P_p was reached, after which, P_c was raised to the target confining pressure. For high temperature experiments, the temperature was then increased to the target temperature (T_{set}) over the course of 2 h, controlled using a PID Omega controller which used a J-type thermocouple in contact with the top forcing block as an input. To account for temperature variations along the length of the sample assembly, calibration tests were performed to determine the temperature at the sample interface relative to the control temperature. For these tests, we monitored the temperature at the interface between the top and bottom forcing blocks (sample location) while controlling temperature from the top forcing block (Figure S1). Reported temperatures (T_{samp}) are corrected to account for this temperature difference to reflect the true temperature at the gouge layer and are plotted using the mean temperature during the experiment. For room temperature experiments, samples were allowed to equilibrate at the target P_c and P_p for 2 h for consistency. This equilibration time allowed for further compaction prior to the beginning of the run-in.

After equilibration, the piston was advanced at a rate of 10 μm/s for a run-in of ~1–2 mm. Triaxial experiments consisted of velocity-stepping tests with axial velocities varying between 1–100 μm/s (velocities on the shear interface varying between 1.414–141.4 μm/s). Displacement during experiments was measured using an external LVDT (resolution ±0.1 μm). Axial load was measured using an external load cell with a resolution of 0.2 MPa and was corrected for pressure-dependent piston friction (Figure S2). Confining pressure was decreased by servo control throughout the experiment to account for the decrease in contact area with increasing displacement (He et al., 2006). In this way, normal stress was held nearly constant. Due to the 45˚ saw-cut configuration, normal stress (σ_N) and shear stress (τ) during experiments were calculated as

$$\sigma_N = \frac{\sigma_1 + P_c}{2} \quad (1a)$$

$$\tau = \frac{\sigma_1 - P_c}{2} \quad (1b)$$

where σ_1 is the measured axial stress. Friction ($\mu=\tau/\sigma$) was corrected for jacket strength by subtracting the displacement-dependent frictional strength of the assembly jacket. Multiple jacket strength tests indicated that the displacement-dependent jacket strength increases with increasing confining pressure, but is insensitive to temperature at the range of temperatures tested here. Displacement in all figures reflects the elastic-corrected displacement along the shear surface (45˚ to the measured axial displacement). We note that, due to the 45˚ saw-cut configuration, normal stress is a function of axial load, which necessarily changes during velocity steps. The change in effective stress during all velocity steps in this study was < 1 MPa. We more fully discuss the implications of this normal stress step in Section 3.4.

3.3. Plate-rate Deformation Experiments

Plate-rate experiments were conducted in order to test the frictional behavior of the gouge at near plate-rates using a Giesa RS5 direct shear apparatus (Figure 2b). Gouge was mixed with brine to create a paste, which was placed into the sample cell and cold pressed in a 25 mm diameter, 30 mm height cylinder. The act of shearing cuts the sample cylinder perpendicular to its axis, so that deformation was accommodated by sliding the two halves past each other rather than by shear distributed throughout the entire cylinder. These experiments were conducted at room temperature and saturated with seawater under atmospheric pressure, but no controlled pore fluid pressure was applied. Normal stress was applied using a vertical ram with resolution of 0.15 kPa. After initial application of 10 MPa normal stress, the sample was allowed to compact overnight (~18 h). Pore fluid remained in communication with the sample through stainless steel frits (5 mm thick, permeability of 10^{-13} m^2) in the bottom plate with the top plate in communication with the atmosphere. During this time the compaction rate, determined as the change in sample height over time, became negligible so that it can be assumed that pore fluid pressure dissipates, and σ_{eff} is taken to be

equivalent to the applied stress. To account for the effect of evaporation on the salinity of the pore fluid brine, the fluid bath was resupplied with DI water throughout the experiment.

Initial run-in was achieved by displacing the top plate relative to the bottom plate at a sliding velocity of 10 μm/s. After steady-state friction was achieved, the slip velocity was decreased to 1.7 nm/s (equivalent to 5.3 cm/yr as observed at Hikurangi), followed by series of velocity steps (Table 1). Shear stress was monitored using a horizontal load cell with resolution of 0.3 kPa.

3.4. Determining rate-and-state friction parameters

Friction (μ) was determined as the ratio of shear stress to effective stress:

$$\mu = \frac{\tau}{\sigma_{eff}} = \frac{\tau}{\sigma_N - P_p} \quad (2).$$

Velocity-dependence of friction is described as *a*–*b*, where *a* and *b* are dimensionless constants determined through analysis of velocity-step data. Velocity-steps in the biaxial experiments (BRAVA and the plate-rate experiments) were analyzed using the rate-and-state friction formulation, where friction is described as:

$$\mu = \mu_0 + aln\left(\frac{V}{V_0}\right) + b_1\left(\frac{V_0\theta_1}{D_{c1}}\right) + b_2\left(\frac{V_0\theta_2}{D_{c2}}\right) \quad (3a)$$

and the state variable can be defined as

$$\frac{d\theta_{1,2}}{dt} = 1 - \frac{V\theta}{D_{c1,2}} \quad (3b)$$

or

$$\frac{d\theta_{1,2}}{dt} = -\frac{V\theta}{D_{c1,2}} ln\left(\frac{V\theta}{D_{c1,2}}\right) \quad (3c)$$

where μ_0 is the friction coefficient prior to a velocity-step, V_0 and V are the sliding velocities prior to and after the velocity-step, respectively (μm/s), θ_1 and θ_2 are the state parameters (s), and D_{c1} and D_{c2} are the critical slip distance (μm) (Dieterich, 1979; Marone, 1998; Ruina, 1983). These parameters were determined using a least-squares iterative inversion (Reinen and Weeks, 1993; Tables S1–S2). We model velocity steps using both the Dieterich (aging;

Eq 3b) and Ruina (slip; Eq 3c) state evolution laws. However, fits yield indistinguishable results (e.g. Figure S3, Tables S1–S2) and we plot RSF parameters determined using the Dieterich law.

In the triaxial deformation experiments, due to the sample geometry, σ_{eff} changes with a velocity step. Because of this, velocity-dependence of friction in these experiments was modeled using an alternative evolution of the state variable that takes into account changing normal stress during the velocity steps (Hong and Marone, 2005; Linker and Dieterich, 1992; Perfettini et al., 2001):

$$\frac{d\theta}{dt} = 1 - \frac{V\theta}{D_c} - \alpha\frac{\theta}{b\sigma}\frac{d\sigma}{dt} \quad , \quad \alpha = \frac{\Delta\tau/\sigma}{\ln(\frac{\sigma}{\sigma_0})} \tag{3d}$$

or

$$\frac{d\theta}{dt} = -\frac{V\theta}{D_c}\ln\left(\frac{V\theta}{D_c}\right) - \alpha\frac{\theta}{b\sigma}\frac{d\sigma}{dt} \quad , \quad \alpha = \frac{\Delta\tau/\sigma}{\ln(\frac{\sigma}{\sigma_0})} \tag{3f}$$

where α is the normalized frictional response to a step in normal stress. Typically, a normal stress step is considered to have a similar effect as a velocity step, with an increase in normal stress causing an increase in shear stress, which approaches a new steady-state value. Both modeling and experimental studies have shown that α is limited to a value between 0 and steady-state friction, μ_{ss}, after the velocity step or change in σ_N (Hong and Marone, 2005; Perfettini et al., 2001). Thus, for each velocity step, we determined the parameters *a*, *b*, and D_c assuming the end member cases where α=0 and α=μ_{ss}. The changes in σ_{eff} during the velocity steps in our experiments are <1 MPa, and, thus, lower than is normally considered in normal stress stepping experiments and not expected to strongly influence the results reported here. Indeed, for all velocity steps in this study, while RSF parameters determined under these two bounding conditions vary slightly, *a–b* values determined with the two approaches are indistinguishable (Figure S3, Table S1–S2) and we plot only the values obtained using the α=0 case.

4. Results

Performing friction experiments on multiple apparatuses affords us the opportunity, not only to access a wider range of deformation conditions, but also to compare results across labs. We find that steady-state friction values measured at comparable σ_{eff} conditions in the different apparatuses are consistent. The coefficient of friction measured in BRAVA experiments exhibits a peak in friction of 0.4–0.6 and then steadily decreases with increased displacement (Figure 2d). The plate-rate experiments, conducted at σ_{eff}=10 MPa, have friction coefficients of ~0.4 and fall well within the range of friction coefficients measured in the BRAVA experiments, which were conducted at σ_{eff}=1–25 MPa (Figure 3a). Unlike the BRAVA experiments, the plate-rate experiments do not show strain weakening (Figure 2e). One overlapping experiment conducted in the triaxial apparatus at σ_{eff}~26 MPa shows a friction coefficient and *a–b* values that are comparable to the σ_{eff}=25 MPa BRAVA experiment (Figure 3a,b). The triaxial friction coefficient is slightly lower than the value measured in the BRAVA experiments. The gouge layers in the triaxial samples were much thinner than those used in the BRAVA experiments (~1.85 mm at the beginning of triaxial deformation experiments and <1 mm, observed upon recovery). This thinner shearing layer yields a higher shear strain at much shorter displacements (Figure S4). We note that while the final gouge layer thickness in triaxial experiments is <1 mm, it was not possible to recover whole samples which would allow for an accurate measurement of post-experiment layer thickness. Therefore, shear strains plotted in Figure S4 and listed in Table 1 for triaxial experiments use a layer thickness of 1 mm and are minimum estimates.

4.1. Influence of effective stress on friction and velocity dependence

Our data show that friction and velocity-dependence vary as a function of effective stress (Figures 3a,b). This is apparent from initial observations of the friction data for experiments

conducted on the three apparatuses (Figure 2). Friction values in the lower stress experiments conducted on BRAVA are highest (up to ~0.57 for the 1 MPa experiment), and show significant strain weakening. The plate-rate experiments conducted at σ_{eff}=10 MPa show a friction coefficient of ~0.4, which is constant with displacement. High effective stress experiments show overall lower friction coefficients (<0.3).

Velocity-dependence of friction shows a similar pattern, with values decreasing as a function of effective stress (Figure 3b). High effective stress experiments also show less scatter in *a*–*b* values than lower effective stress experiments. We highlight that the plate-rate experiments, conducted at the relatively low effective stress of 10 MPa, show velocity-weakening behavior at sliding velocities <1 μm/s (Figure 3b).

4.2. Influence of temperature on friction and velocity dependence

The temperatures relevant in the shallow portion of the Hikurangi subduction zone have a much smaller impact than σ_{eff} on friction and frictional stability. Experiments conducted at elevated temperatures show higher friction coefficients than those conducted at the same σ_{eff} and lower temperature (Figure 3c). However, this trend becomes less pronounced for higher effective stress experiments. Similarly, we see a slight increase in *a*–*b* with increasing temperature (Figure 3d), though for the highest stress experiments, this trend is much less pronounced.

4.3. Influence of sliding velocity on velocity dependence

Sliding velocity has a strong effect on friction velocity dependence at low effective stresses (Figure 4). At σ_{eff}=1 MPa, *a*–*b* ranges from 0.007 for the 1–3 μm/s velocity step to 0.021 for the 100–300 μm/s velocity step. At higher effective stresses of 5–25 MPa, *a*–*b* remains more constant over the range of velocities tested, with values from 0.002–0.011, although the trend of increasing *a*–*b* with increasing sliding velocity is still apparent. In the

~26 MPa experiment conducted on the triaxial apparatus, *a–b* values are close to those observed in the 25 MPa experiment on BRAVA, though two points are slightly lower, and there is no clear velocity dependence (Figure 4). In the plate-rate experiments, conducted at σ_{eff}=10 MPa, we see a transition to velocity-weakening behavior below an upstep velocity of ~1 μm/s (Figure 4). We note that, while some work has shown that transient increases in pore fluid pressure can lead to apparently lower values of *a–b* (Faulkner et al., 2018), we see slight dilation during our velocity steps, suggesting that any transient effect is one of a drop in pore fluid pressure (Figure S5).

4.4. Variation in RSF Parameters

We see a systematic decrease with increasing effective stress in *a* values, as well as a slight increase with increasing temperature (Figure 5a,b). In all experiments conducted in this study, we see mostly low values of *b* with no clear trend as a function of effective stress or temperature (Figure 5c,d). Scatter in *b* appears to decrease with increasing effective stress, implying a diminishing impact of changing sliding velocity on the *b* value with increasing effective stress. A similar pattern is seen in D_c, with no clear trend as a function of effective stress or temperature, though the highest values of D_c at each effective stress value show a decreasing trend with increasing effective stress (Figure 5e,f).

4.5. Experimental SSEs

Two slow slip events are observed in the plate-rate experiment B628 (Figure 2d). The first SSE begins with an accumulation of stress, accompanied by a reduction in slip velocity along the sample (Figure 6a,e). A stress drop ($\Delta\tau$) of ~0.028 MPa is accommodated over ~1.5 h. This stress drop is accompanied by a doubling of the slip velocity from the imposed slip velocity of 1.7 nm/s to 4 nm/s (Figure 6e). The second SSE also begins with an

accumulation of shear stress accompanied by a slip deficit accumulation (Figure 6d). Again, the stress drop of ~0.026 MPa occurs over ~2 h (Figure 6b). This stress drop is accompanied by another peak in slip velocity of 4 nm/s (Figure 6f).

5. Discussion

5.1. Mineralogical controls on friction and stability

While the sediment from ODP 1124C used in this study is largely composed of calcite (43 wt%) with smaller contributions of phyllosilicates (20 wt%), quartz (9 wt%), and feldspars (15 wt%), the low friction coefficients (<0.21 for σ_{eff} > 25 MPa) observed in our experiments show the influence of clays, which are known to exhibit low friction (Byerlee, 1978; Shimamoto and Logan 1981; Morrow et al., 1992b; Brown et al., 2003; Ikari et al, 2009; Saffer et al., 2001; Saffer and Marone, 2003). This is consistent with previous studies in talc/calcite mixtures which have demonstrated that the phyllosilicate fraction dominates frictional behavior at talc contents of at least 20 wt% (Giorgetti et al., 2015). Other studies comparing the frictional behavior of clay/quartz mixtures show that, while the clay component controls the gouge friction only at concentrations >50%, a transition towards clay-like low frictional strength begins at clay concentrations of ~20% (Saffer and Marone, 2003; Crawford et al., 2008; Ikari et al., 2007; Tembe et al., 2010). We note that, while these previous studies provide a reference for the behavior of bimineralic mixtures of clay and quartz, the sediment tested here is a more complicated mixture of different types of clays, calcite, quartz, and feldspar. Indeed, previous work measuring the frictional properties of input sediments from other subduction zones has shown a wide range of both frictional strength and velocity dependence in these natural compositions (Ikari et al., 2009, 2013, 2015; Ikari and Saffer, 2011; Kopf and Brown, 2003; Saito et al., 2013), with higher clay contents usually correlating with low friction coefficients and velocity-strengthening behavior. We are unable to definitively determine which exact mineral species controls the

frictional strength and stability in our experiments. However, the fact that the behavior observed in this sediment is similar to previous observations in clays suggests that the clay fraction acts as the primary control on friction. Differences in the behavior of clay mixtures highlight the need for more friction experiments on natural gouges with complicated mineralogies.

One striking observation from our experiments is the strong dependence of friction and frictional stability on effective stress (Figure 3a,b). The dramatic reduction in friction coefficient with increasing effective stress is consistent with previous observations of the frictional behavior of smectite-rich gouge (Saffer et al., 2001; Saffer and Marone, 2003). Saffer and Marone (2003) showed that the friction coefficient of smectite decreases to values ≤0.1 at effective stresses above 30–40 MPa (Figure 3a). They suggest two main mechanisms for this transition, which happens at significantly lower stresses than expected for most minerals. The first mechanism is that the low friction coefficient is controlled by a weak, hydrated interlayer in the clay structure (Bird, 1984). At higher stresses, this water could be expelled, leading to locally elevated pore fluid pressures (Moore and Lockner, 2007; Morrow et al., 2017; Faulkner et al., 2018). Alternatively, the transition to pressure-insensitive creep (indicated by the low friction coefficients measured in the high effective stress experiments) could be the result of a transition to achieving nearly full contact between clay grains (real area of contact ≈ nominal area of contact) at ~30 MPa (Saffer and Marone, 2003). This would be expected to happen at a lower stress for clays than other minerals as a result of the platy structure of the clays and is supported in our experiments by the low values of b observed in all high stress experiments (Figure 5c). The evolution effect, b, is interpreted to indicate the change in contact area between grains in a frictionally sliding material (Dieterich and Kilgore, 1994). For platy minerals like clays, the contact area is already maximized at a relatively low stress, leading to low or negative values of b as seen in our experiments (Ikari

et al., 2016). We note that the evolution of *a–b* to lower values with increasing effective stress and to higher values with increasing temperature is driven largely by changes in the direct effect, *a*. Decreases in *a* with increasing effective stress could be the result of more efficient alignment of the clay fabric, with the disruption of that fabric during a velocity step being more dramatic at lower σ_{eff}.

We note that frictional strength in our overlapping experiments in BRAVA and on the triaxial deformation apparatus differ slightly (Figure 2, ~25 MPa effective stress). This could be the result of the longer time and higher effective stresses during the initial compaction or thinner gouge layers leading to higher strain for the triaxial experiments (near the stress applied during the experiment), which could lead greater fabric development (i.e. the alignment of phyllosilicate grains) in the gouge prior to deformation (Haines et al., 2009, 2013). The BRAVA experiments all show strain weakening throughout and by the end of the experiment the steady-state friction value is nearly identical to the steady-state value measured in the triaxial deformation apparatus (Figure 2). Previous experiments have demonstrated that well-developed fabric can cause low friction in phyllosilicate-rich materials (Collettini et al., 2009; Ikari et al., 2011b; Tesei et al., 2015).

However, it is clear that strain weakening cannot fully explain the difference in friction coefficient between the BRAVA and the triaxial experiments at σ_{eff}~25 MPa because we do not see the same strain weakening pattern in the triaxial experiments. Haines et al. (2009) demonstrated that compaction promotes fabric development, particularly at high normal stresses, though this effect is minimal compared to the effect of strain on fabric development in dry, clay-rich samples. It is possible that the addition of fluids, longer compaction times, and higher effective stresses during pre-compaction could lead to more efficient initial fabric development in the triaxial experiments, leading to a lower measured friction. However, further tests comparing fabric development in the early stages of experiments in these two

configurations are necessary to test this hypothesis. Alternatively, it is possible that differences in strain localization in the experiments conducted on the triaxial deformation apparatus and BRAVA (e.g. from differences in sample configuration such as teeth size on the forcing blocks) could lead to differences in fabric development early in the experiments. Due to the lack of well-recovered gouge layers after the triaxial deformation experiments, we are unable to perform microstructural analysis to test this hypothesis.

5.2. Implications for the Hikurangi subduction zone

In Figure 7, we plot the friction and velocity-dependence of samples deformed at effective stress and temperature conditions expected on the Hikurangi plate boundary, assuming a hydrostatic effective stress gradient (15 MPa/km) and a geotherm of 10 ˚C/km (Table 1; McCaffrey et al., 2008). We see a reduction in friction coefficient and $a–b$ with increasing depth. We also note that our plate-rate experiments, which showed velocity-weakening behavior below 1 μm/s, were conducted at 10 MPa, an effective stress where we observe significant velocity strengthening in the biaxial experiments (Figure 3a). Assuming that the trends in frictional strength and velocity-dependence with σ_{eff} hold true at lower sliding velocities, velocity-weakening behavior could be expected in this gouge when deformed at plate-rate velocities at depths of ~2–10 km. However, with increasing pressure and temperature, processes such as pressure solution have a greater influence on slip behavior (e.g. Bos and Spiers, 2000, 2001; Bos et al, 2000; Niemeijer and Spiers, 2005; Moore et al., 2007). Slow experiments at higher pressure and temperature conditions are necessary to determine the evolution of μ and $a–b$ with increasing depth at plate-rate velocities.

Our results indicate that shallow slow slip in the Hikurangi Trench could be hosted in the sedimentary material tested here. At velocities in the range of 1–300 μm/s, material is velocity-strengthening at low stresses and room temperature, with some velocity-neutral

behavior at higher stresses and temperatures, consistent with the occurrence of shallow SSEs at depths below 2 km (Figure 7)(Wallace et al., 2017). Though the consistently velocity-strengthening nature of the gouge, particularly at the shallowest depths, supports the occurrence of aseismic slip in this material, our plate-rate experiments show that below the cutoff velocity of ~1 μm/s (three orders of magnitude larger than the plate convergence rate at Hikurangi), this lithology is velocity-weakening (Figure 4). This potentially unstable behavior at low effective stress implies that slow slip could extend even to shallower depths within faults of this composition. The importance of this transition to unstable behavior at low sliding velocities is further supported by numerical modeling studies that generate slow slip events in subduction zones by using a cutoff velocity at least two orders of magnitude larger than the plate convergence rate (e.g. Shibazaki and Iio, 2003; Matsuzawa et al., 2010; Hawthorne and Rubin, 2013). We note that the cutoff velocity of ~1 μm/s that we see in the plate-rate experiments is higher than the average slip velocities of the SSEs observed in the northern Hikurangi subduction zone (1–3 cm/day or ~0.12–0.35 μm/s; Figure 4). These values are also higher than the slip velocities observed in the experimental SSEs (~4 nm/s). This observation highlights that it is the frictional stability, which includes effects of effective stress together with the stiffness of the fault and the loading system (Leeman et al., 2016; Scuderi et al., 2016) that controls the behavior of slip events and not the friction velocity dependence alone. Future work on lab SSEs could yield better understanding of how rate-state properties translate into unstable behavior.

We note that elevated temperatures within the range expected for shallow SSEs at Hikurangi (McCaffrey et al., 2008) do not exert a strong control on either friction or frictional stability in this material, though the highest temperatures tested here are modest compared to the temperatures at which velocity-weakening behavior has previously been observed in clays (den Hartog et al., 2012a, 2012b; Moore et al., 1989, 1986, 1983). However, calcite is

expected to exhibit velocity-weakening behavior at the highest temperatures tested here (Ikari et al., 2013b; Kurzawski et al., 2016; Verberne et al., 2014a, 2014b, 2013). Therefore, we suggest it does not control the frictional behavior of sediment subducting at the shallow portions of the Hikurangi Trench at velocities higher than ~1 μm/s. At lower velocities relevant to SSEs, where mechanisms such as pressure solution might be active, calcite could play a larger role in deformation style (Verberne et al, 2013, 2014b; Zhang et al., 2010) (Figure 4).

In addition to SSEs, the northern Hikurangi margin also relieves strain through tsunami earthquakes. These earthquakes, though slower in rupture velocity than regular earthquakes (<1 km/s), are expected to slip at velocities significantly faster than SSEs (Polet and Kanamori, 2000). The ~M 7 1947 Offshore Poverty Bay and Tolaga Bay earthquakes ruptured in the shallow portion of the subduction zone where SSEs have been observed (Bell et al., 2014). Although the material tested here shows velocity-strengthening behavior at velocities above 1 μm/s (indicating that earthquakes are unlikely to nucleate in these sediments), our work does not preclude the possibility of earthquake rupture propagation through these sediments. We note that compositional heterogeneity of the subducting sediment package could play a clear role in the nucleation of both SSEs and tsunami earthquakes, both of which have been shown to be spatially associated with the presence of subducting seamounts (Bell et al., 2010, 2014; Wallace et al., 2016). Previous work has suggested that elevated carbonate concentrations on seamounts could lead to more frictionally unstable behavior (Ikari et al., 2013). Future experiments using sediments from IODP Expedition 375, which recovered sedimentary inputs into the Hikurangi Trench, will provide additional context about the frictional controls on SSEs and earthquakes at this subduction zone.

6. Conclusions

Our experiments show that even for a lithology with only 20 wt% phyllosilicates, the clay fraction of the gouge controls the frictional behavior. We see that frictional strength decreases dramatically with increasing effective stress, starting at an estimated depth of ~2–3 km, implying pressure-independent shear stress at the depths where shallow SSEs occur in the Hikurangi subduction zone. At the temperatures expected in the shallow subduction zone at Hikurangi, temperature does not exert a strong control on friction or frictional stability. Plate-rate velocities promote velocity-weakening behavior, even at low stresses and temperatures, and suggest that the sediment subducting at Hikurangi is capable of hosting SSEs without fluid overpressure. These experiments highlight that the normal stress, temperature, and sliding velocities expected in the region of Hikurangi margin slow slip events are favorable for velocity-neutral frictional behavior. Small perturbations in these conditions could push a fault into instability.

Acknowledgements, Samples, and Data

Samples for this study were provided by the International Ocean Discovery Program (IODP). We thank the curatorial staff at the Gulf Coast Repository for help obtaining samples. Funding for this project was provided by an NSF GRFP (DGE-11-44155) to H. Rabinowitz, the European Research Council (ERC) under the European Union's Horizon 2020 research and innovation program (grant agreement #714430) to M. Ikari, and ERC Grant GLASS project (grant agreement #259256) to C. Collettini. Many thanks to Ted Koczynski for help with the triaxial deformation apparatus. We thank Laura Wallace and Demian Saffer as well as an anonymous reviewer for helpful comments. Data presented in this work are listed in the supplementary tables.

References

Araki, E., Saffer, D.M., Kopf, A.J., Wallace, L.M., Kimura, T., Machida, Y., Ide, S., Davis, E., 2017. Recurring and triggered slow-slip events near the trench at the Nankai Trough subduction megathrust. *Science* 356(6343), 1157–1160. doi: 10.1126/science.aan3120

Audet, P., Bostock, M.G., Christensen, N.I., Peacock, S.M., 2009. Seismic evidence for overpressured subducted oceanic and megathrust fault sealing. *Nature* 457(7225), 76. doi: 10.1038/nature07650

Bassett, D., Sutherland, R., Henrys, S., 2014. Slow wavespeeds and fluid overpressure in a region of shallow geodetic locking and slow slip, Hikurangi subduction margin, New Zealand. *Earth and Planetary Science Letters* 389, 1–13. doi: 10.1016/j.epsl.2013.12.021

Beavan, J., Wallace, L., Fletcher, H., Douglas, A., 2007. Slow slip events on the Hikurangi subduction interface, New Zealand. In: *Dynamic Planet* (pp. 438–444). Springer, Berlin, Heidelberg.

Bell, R., Holden, C., Power, W., Wang, X., Downes, G., 2014. Hikurangi margin tsunami earthquake generated by slow seismic rupture over a subducted seamount. *Earth and Planetary Science Letters* 397, 1–9. doi: 10.1016/j.epsl.2014.04.005

Bell, R., Sutherland, R., Barker, D.H.N., Henrys, S., Bannister, S., Wallace, L., Beavan, J., 2010. Seismic reflection character of the Hikurangi subduction interface, New Zealand, in the region of repeated Gisborne slow slip events. *Geophysical Journal International* 180(1), 34–48. doi: 10.1111/j.1365-246X.2009.04401.x

Bird, P., 1984. Hydration-phase diagrams and friction of montmorillonite under laboratory and geologic conditions, with implications for shale compaction, slope stability, and strength of fault gouge. *Tectonophysics* 107(3–4), 235–260. doi: 10.1016/0040-1951(84)90253-1

Bos, B., Spiers, C.J., 2000. Effect of phyllosilicates on fluid-assisted healing of gouge-bearing faults. Earth and Planetary Science Letters 184(1), 199–210. doi: 10.1016/S0012-821X(00)00304-6

Bos, B., Peach, C.J., Spiers, C.J., 2000. Frictional-viscous flow of simulated fault gouge caused by the combined effects of phyllosilicates and pressure solution. *Tectonophysics* 327(3–4). doi: 10.1016/S0040-1951(00)00168-2

Bos, B., Spiers, C.J., 2001. Experimental investigation into the microstructural and mechanical evolution of phyllosilicate-bearing fault rock under conditions favouring pressure solution. *Journal of Structural Geology* 23(8), 1187–1202. doi: 10.1016/S0191-8141(00)00184-X

Brown, K.M., Kopf, A., Underwood, M.B. and Weinberger, J.L., 2003. Compositional and fluid pressure controls on the state of stress on the Nankai subduction thrust: A weak plate boundary. *Earth and Planetary Science Letters* 214(3–4), 589–603. doi: 10.1016/S0012-821X(03)00388-1

Buijze, L., Niemeijer, A.R., Han, R., Shimamoto, T., Spiers, C.J., 2017. Friction properties and deformation mechanisms of halite(-mica) gouges from low to high sliding velocities. *Earth and Planetary Science Letters* 458, 107–119. doi: 10.1016/j.epsl.2016.09.059

Byerlee, J., 1978. Friction of Rocks. In *Rock friction and earthquake prediction* (pp. 615–626) Birkhäuser, Basel.

Carter, R.M., McCave, I.N., Richter, C., Carter, L., Aita, Y., Buret, C., Di Stefano, A., Fenner, J., Fothergill, P., Gradstein, F., Hall, I., Handwerger, D., Harris, S., Hayward, B., Hu, S., Joseph, L., Keun Khim, B., Lee, Y., Millwood, L., Rinna, J., Smith, G., Suzuki, A., Weedon, G., Wei, K., Wilson, G., Winkler, A., 2000. Volume 181 Initial Reports: Southwest Pacific Gateways.

Collettini, C., Di Stefano, G., Carpenter, B., Scarlato, P., Tesei, T., Mollo, S., Trippetta, F., Marone, C., Romeo, G., Chiaraluce, L., 2014. A novel and versatile apparatus for brittle rock deformation. *International Journal of Rock Mechanics and Mining Sciences* 66, 114–123. doi: 10.1016/j.ijrmms.2013.12.005

Collettini, C., Niemeijer, A., Viti, C., Marone, C., 2009. Fault zone fabric and fault weakness. *Nature* 462, 907–910. doi: 10.1038/nature08585

Crawford, B.R., Faulkner, D.R., and Rutter, E.H., 2008. Strength, porosity, and permeability development during hydrostatic and shear loading of synthetic quartz-clay fault gouge. *Journal of Geophysical Research: Solid Earth* 113(B3). doi: 10.1029/2006JB004634

Davy, B., Wood, R., 1994. Gravity and Magnetic Modeling of the Hikurangi Plateau. *Marine Geology* 118(1–2), 139–151. doi: 10.1016/0025-3227(94)90117-1

den Hartog, S.M., Niemeijer, A.R., Spiers, C.J., 2012a. New constraints on megathrust slip stability under subduction zone P–T conditions. *Earth and Planetary Science Letters* 353–354, 240–252. doi: 10.1016/j.epsl.2012.08.022

den Hartog, S.M., Peach, C.J., de Winter, D.A.M., Spiers, C.J., Shimamoto, T., 2012b. Frictional properties of megathrust fault gouges at low sliding velocities: New data on effects of normal stress and temperature. *Journal of Structural Geology* 38, 156–171. doi: 10.1016/j.jsg.2011.12.001

Delahaye, E.J., Townend, J., Reyners, M.E., and Rogers, G., 2009. Microseismicity but no tremor accompanying slow slip in the Hikurangi subduction zone, New Zealand. *Earth and Planetary Science Letters*, 277(1–2), 21–28. doi: 10.1016/j.epsl.2008.09.038

Dieterich, J.H., 1979. Modeling of rock friction: 1. Experimental results and constituve equations. *Journal of Geophysical Research: Solid Earth* 84(B5), 2161–2168. doi: 10.1029/JB084iB05p02161

Dieterich, J.H., Kilgore, B.D., 1994. Direct observation of frictional contacts: New insights for state-dependent properties. *Pure and Applied Geophysics*. 143(1–3), 283–302.

Doser, D.I., Webb, T.H., 2003. Source parameters of large historical (1917-1961) earthquakes , North Island, New Zealand. *Geophysical Journal International*. 152(3), 795–832. doi: 10.1046/j.1365-246X.2003.01895.x

Douglas, A., Beavan, J., Wallace, L., Townend, J., 2005. Slow slip on the northern Hikurangi subduction interface, New Zealand. *Geophysical Research Letters* 32(16). doi: 10.1029/2005GL023607

Dragert, G., Wang, K., James, T.S., 2001. A silent slip event on the deeper Cascadia subduction interface. *Science*. 292(5521), 1525–1528. doi: 10.1126/science.1060152

Dragert, H., Wang, K., Rogers, G., 2004. Geodetic and seismic signatures of episodic tremor and slip in the northern Cascadia subduction zone. *Earth, Planets, and Space* 56(12), 1143–1150. doi: 10.1186/BF03353333

Ellis, S., Fagereng, Å., Barker, D., Henrys, S., Saffer, D., Wallace, L., Williams, C., Harris, R., 2015. Fluid budgets along the northern Hikurangi subduction margin, New Zealand: The effect of a subducting seamount on fluid pressure. *Geophysical Journal International* 202(1), 277–297. doi: 10.1093/gji/ggv127

Faulkner, D.R., Sanchez-Roa, C., Boulton, C. and den Hartog, S.A.M., 2018. Pore Fluid Pressure Development in Compacting Fault Gouge in Theory, Experiments, and Nature. *Journal of Geophysical Research: Solid Earth* 123(1), 226–241. doi: 10.1002/2017JB015130

Faulkner, D.R., Mitchell, T.M., Behnsen, J., Hirose, T., Shimamoto, T., 2011. Stuck in the mud? Earthquake nucleation and propagation through accretionary forearcs. *Geophysical Research Letters* 38(18). doi: 10.1029/2011GL048552

Giorgetti, C., Carpeter, B.M., Collettini, C., 2015. Frictional behavior of talc-calcite mixtures. *Journal of Geophysical Research: Solid Earth* 120(9), 6614–6633. doi: 10.1002/2015JB011970

Haines, S.H., Van Der Pluijm, B.A., Ikari, M.J., Saffer, D.M., Marone, C., 2009. Clay fabric intensity in natural and artificial fault gouges : Implications for brittle fault zone processes and sedimentary basin clay fabric evolution. *Journal of Geophysical Research: Solid Earth* 114(B5). doi: 10.1029/2008JB005866

Haines, S.H., Kaproth, B., Marone, C., Saffer, D. and van der Pluijm, B., 2013. Shear zones in clay-rich fault gouge: A laboratory study of fabric development and evolution. *Journal of Structural Geology* 51, 206–225. doi: 10.1016/j.jsg.2013.01.002

Hawthorne, J.C., Rubin, A.M., 2013. Laterally propagating slow slip events in a rate and state friction model with a velocity-weakening to velocity-strengthening transition. *Journal of Geophysical Research: Solid Earth* 118(7). doi: 10.1002/jgrb.50261

Hamling, I.J., Wallace, L.M., 2015. Silent triggering: Aseismic crustal faulting induced by a subduction slow slip event. *Earth and Planetary Science Letters* 421, 13–19. doi: 10.1016/j.epsl.2015.03.046

He, C., Yao, W., Wang, Z., Zhou, Y., 2006. Strength and stability of frictional sliding of gabbro gouge at elevated temperatures. *Tectonophysics* 427(1–4), 217–229. doi: 10.1016/j.tecto.2006.05.023

Hong, T., Marone, C., 2005. Effects of normal stress perturbations on the frictional properties of simulated faults. *Geochemistry, Geophysics, Geosystems* 6(3). doi: 10.1029/2004GC000821

Hyndman, R.D., Yamano, M., Oleskevich, D.A., 1997. The seismogenic zone of subduction thrust faults. *Island Arc* 6(3), 244–260. doi: 10.1111/j.1440-1738.1997.tb00175.x

Ide, S., Beroza, G.C., Shelly, D.R., Uchide, T., 2007. A scaling law for slow earthquakes. *Nature* 447(7140), 76. doi: 10.1038/nature05780

Ikari, M.J., Ito, Y., Ujiie, K., Kopf, A.J., 2015. Spectrum of slip behaviour in Tohoku fault zone samples at plate tectonic slip rates. *Nature Geoscience* 8(11), 870–874. doi: 10.1038/ngeo2547

Ikari, M.J., Kopf, A.J., 2017. Seismic potential of weak, near-surface faults revealed at plate tectonic slip rates. *Science Advances* 3(11), e1701269. doi: 10.1126/sciadv.1701269

Ikari, M.J., Carpenter, B.M., and Marone, C., 2016. A microphysical interpretation of rate- and state-dependent friction for fault gouge. *Geochemistry, Geophysics, and Geosystems*, 17(5), 1660–1677. doi: 10.1002/2016GC006286

Ikari, M.J., Kameda, J., Saffer, D.M., Kopf, A.J., 2015. Strength characteristics of Japan Trench borehole samples in the high-slip region of the 2011 Tohoku-Oki earthquake. *Earth and Planetary Science Letters*, 412, 35–41. doi: 10.1016/j.epsl.2014.12.014

Ikari, M.J., Marone, C., Saffer, D.M., 2011a. On the relation between fault strength and frictional stability. *Geology* 39(1), 83–86. doi: 10.1130/G31416.1

Ikari, M.J., Marone, C., Saffer, D.M., Kopf, A.J., 2013a. Slip weakening as a mechanism for slow earthquakes. *Nature Geoscience* 6(6), 468–472. doi: 10.1038/ngeo1818

Ikari, M.J., Niemeijer, A.R., Marone, C., 2011b. The role of fault zone fabric and lithification state on frictional strength, constitutive behavior, and deformation microstructure. *Journal of Geophysical Research: Solid Earth* 116(B8). doi: 10.1029/2011JB008264

Ikari, M.J., Niemeijer, A.R., Spiers, C.J., Kopf, A.J., Saffer, D.M., 2013b. Experimental evidence linking slip instability with seafloor lithology and topography at the Costa Rica convergent margin. *Geology* 41(8), 891–894. doi: 10.1130/G33956.1

Ikari, M.J., Saffer, D.M., 2011. Comparison of frictional strength and velocity dependence between fault zones in the Nankai accretionary complex. *Geochemistry, Geophysics, Geosystems* 12(4). doi: 10.1029/2010GC003442

Ikari, M.J., Saffer, D.M., Marone, C., 2007. Effect of hydration state on the frictional properties of montmorillonite-based fault gouge. *Journal of Geophysical Research: Solid Earth* 112(B6). doi: 10.1029/2006JB004748

Ikari, M.J., Saffer, D.M., Marone, C., 2009a. Frictional and hydrologic properties of a major splay fault system, Nankai subduction zone. *Geophysical Research Letters* 36(20). doi: 10.1029/2009GL040009

Ikari, M.J., Saffer, D.M., Marone, C., 2009b. Frictional and hydrologic properties of clay-rich fault gouge. *Journal of Geophysical Research: Solid Earth* 114(B5). doi: 10.1029/2008JB006089

Ito, Y., Hino, R., Kido, M., Fujimoto, H., Osada, Y., Inazu, D., Ohta, Y., Iinuma, T., Ohzono, M., Miura, S., Mishina, M., Suzuki, Tsuji, T., Ashi, J., 2013. Episodic slow slip events in the Japan subduction zone before the 2011 Tohoku-Oki earthquake. *Tectonophysics* 600, 14–26. doi: 10.1016/j.tecto.2012.08.022

Ito, Y., Obara, K., 2006. Very low frequency earthquakes within accretionary prisms are very low stress-drop earthquakes. *Geophysical Research Letters* 33(9). doi: 10.1029/2006GL025883

Kato, A., Obara, K., Igarashi, T., Tsuruoka, H., Nakagawa, S., Hirata, N., 2012. Propagation of Slow Slip Leading Up to the 2011 Mw 9.0 Tohoku-Oki Earthquake. *Science* 335(6069), 705–708. doi: 10.1126/science.1215141

Kitajima, H., Saffer, D.M., 2012. Elevated pore pressure and anomalously low stress in regions of low frequency earthquakes along the Nankai Trough subduction megathrust. *Geophysical Research Letters* 39(23). doi: 10.1029/2012GL053793

Kopf, A., Brown, K.M., 2003. Friction experiments on saturated sediments and their implications for the stress state of the Nankai and Barbados subduction thrusts. *Marine Geology* 202(3–4), 193–210. doi: 10.1016/S0025-3227(03)00286-X

Kurzawski, R.M., Stipp, M., Niemeijer, A.R., Spiers, C.J., Behrmann, J.H., 2016. Earthquake nucleation in weak subducted carbonates. *Nature Geoscience* 9(9), 717–722. doi: 10.1038/ngeo2774

Leeman, J.R., Saffer, D.M., Scuderi, M.M., and Marone, C., 2016. Laboratory observations of slow earthquakes and the spectrum of tectonic fault slip modes. *Nature Communications* 7, 11104, doi:10.1038/ncomms11104.

Lewis, K.B., Collot, J.Y., Lallemand, S.E., 1998. The dammed Hikurangi Trough: A channel-fed trench blocked by subducting seamounts and their wake avalanches (New Zealand-France GeodyNZ Project). *Basin Research* 10(4), 441–468. doi: 10.1046/j.1365-2117.1998.00080.x

Linker, M.F., Dieterich, J.H., 1992. Effects of variable normal stress on rock friction: Observations and constitutive equations. *Journal of Geophysical Research: Solid Earth* 97(B4), 4923–4940. doi: 10.1029/92JB00017

Matsuzawa, T., Hirose, H., Shibazaki, B., and Obara, K., 2010. Modeling short-and long-term slow slip events in the seismic cycles of large subduction earthquakes. *Journal of Geophysical Research: Solid Earth* 115(B12). doi: 10.1029/2010JB007566

Marone, C., 1998. Laboratory-Derived Friction Laws and Their Application To Seismic Faulting. *Annual Review of Earth Planetary Sciences* 26(1), 643–696. doi: 10.1146/annurev.earth.26.1.643

McCaffrey, R., Wallace, L.M., Beavan, J., 2008. Slow slip and frictional transition at low temperature at the Hikurangi subduction zone. *Nature Geoscience* 1(5), 316–320. doi: 10.1038/ngeo178

Melbourne, T.I., Webb, F.H., 2002. Precursory transient slip during the 2001 Mw=8.4 Peru earthquake sequence from continuous GPS. Geophys. Res. Lett. 29, 1–4.

Moore, D.E., Lockner, D.A., 2007. Friction of the Smectite Clay Montmorillonite, In: *The*

Seismogenic Zone of Subduction Thrust Faults. New York, New York pp. 317–345.
Moore, J.C. and Saffer, D., 2001. Updip limit of the seismogenic zone beneath the accretionary prism of southwest Japan: An effect of diagenetic to low-grade metamorphic processes and increasing effective stress. *Geology* 29(2), 183–186. doi: 10.1130/0091-7613(2001)029<0183:ULOTSZ>2.0.CO;2
Moore, D.E., Lockner, D.A., 2008. Talc friction in the temperature range 25°–400 °C: Relevance for Fault-Zone Weakening. *Tectonophysics* 449(1–4), 120–132. doi: 10.1016/j.tecto.2007.11.039
Moore, D.E., Lockner, D.A., 2011. Frictional strengths of talc-serpentine and talc-quartz mixtures. *Journal of Geophysical Research: Solid Earth* 116(B1). doi: 10.1029/2010JB007881
Moore, D.E., Summers, R., Byerlee, J.D., 1983. Strengths of clay and non-clay fault gouges at elevated temperatures and pressures, In: *The 24th U.S. Symposium on Rock Mechanics (USRMS)*, College Station, Texas. pp. 489–500.
Moore, D.E., Summers, R., Byerlee, J.D., 1986. The effects of sliding velocity on the frictional and physical properties of heated fault gouge. Pure and Applied Geophysics124(1–2), 31–52. doi: 10.1016/0191-8141(89)90072-2
Moore, D.E., Summers, R., Byerlee, J.D., 1989. Sliding behavior and deformation textures of heated illite gouge. Journal of Structural Geology 11(3), 329–342.
Morrow, C., Radney, B., Byerlee, J., 1992. Frictional strength and the effective pressure law of montmorillonite and illite clays. *International Geophysics* 51, 69–88. doi: 10.1016/S0074-6142(08)62815-6
Morrow, C.A., Moore, D.E., and Lockner, D.A., 2017. Frictional strength of wet and dry montmorillonite. *Journal of Geophysical Research: Solid Earth* 122(5), 3392–3409. doi: 10.1002/2016JB013658
Niemeijer, A.R., Boulton, C., Toy, V.G., Townend, J., Sutherland, R., 2016. Large-displacement, hydrothermal frictional properties of DFDP-1 fault rocks, Alpine Fault, New Zealand: Implications for deep rupture propagation. *Journal of Geophysical Research: Solid Earth* 121, 624–647. doi: 10.1002/2015JB012593
Niemeijer, A., Marone, C., Elsworth, D., 2010. Fabric induced weakness of tectonic faults. *Geophysical Research Letters* 37(3). doi: 10.1029/2009GL041689
Niemeijer, A.R., Spiers, C.J., 2005. Influence of phyllosilicates on fault strength in the brittle-ductile transition: insights from rock analogue experiments. *Geological Society, London, Special Publications* 245(1), 303–327. doi: 10.1144/GSL.SP.2005.245.01.15
Obara, K., 2002. Nonvolcanic deep tremor associated with subduction in southwest Japan. *Science* 296(5573), 1679–1681. doi: 10.1126/science.1070378
Obara, K., Hirose, H., 2006. Non-volcanic deep low-frequency tremors accompanying slow slips in the southwest Japan subduction zone. *Tectonophysics* 417(1–2), 33–51. doi: 10.1016/j.tecto.2005.04.013
Outerbridge, K.C., Dixon, T.H., Schwartz, S.Y., Walter, J.I., Protti, M., Gonzalez, V., Biggs, J., Thorwart, M., Rabbel, W., 2010. A tremor and slip event on the Cocos-Caribbean subduction zone as measured by a global positioning system (GPS) and seismic network on the Nicoya Peninsula, Costa Rica. Journal of Geophysical Research 115(B10). doi: 10.1029/2009JB006845
Ozawa, S., Suito, H., Tobita, M., 2007. Occurrence of quasi-periodic slow-slip off the east coast of the Boso peninsula, Central Japan. *Earth, Planets and Space* 59(12), 1241–1245.
Payero, J.S., Kostoglodov, V., Shapiro, N., Mikumo, T., Iglesias, A., Perez-Campos, X., Clayton, R.W., 2008. Nonvolcanic tremor observed in the Mexican subduction zone. *Geophysical Research Letters* 35(7), L07305. doi: 10.1029/2007GL032877

Pelayo, A.M., Wiens, D.A., Tsunami Earthquakes: Slow Thrust-Faulting Events in the Accretionary Wedge. *Journal of Geophysical Research* 97(B11), 15321–15337. doi: 10.1029/92JB01305

Peng, Z., Gomberg, J., 2010. An integrated perspective of the continuum between earthquakes and slow-slip phenomena. Nature Geoscience 3(9), 599–607. doi: 10.1038/ngeo940

Perfettini, H., Schmittbuhl, J., Rice, J.R., Cocco, M., 2001. Frictional response induced by time-dependent fluctuations of the normal loading. *Journal of Geophysical Research* 106(B7), 13455–13472. doi: 10.1029/2000JB900366

Petschick, R., Kuhn, G., and Gingele, F., 1996. Clay mineral distribution in surface sediments of the South Atlantic: sources, transport, and relation to oceanography. *Marine Geology* 130(3–4), 203–229. doi: 10.1016/0025-3227(95)00148-4

Plank, T., 2014. The Chemical Composition of Subducting Sediments, *Treatise on Geochemistry* 4, 607–629.

Polet, J. and Kanamori, H., 2000. Shallow subduction zone earthquakes and their tsunamigenic potential. *Geophysical Journal International* 142(3), 648–702. doi: 10.1046/j.1365-246x.2000.00205.x

Radiguet, M., Perfettini, H., Cotte, N., Gualandi, A., Valette, B., Kostoglodov, V., Lhomme, T., Walpersdorf, A., Cabral Cano, E., Campillo, M., 2016. Triggering of the 2014 Mw7.3 Papanoa earthquake by a slow slip event in Guerrero, Mexico. *Nature Geoscience* 9(11), 829–833. doi: 10.1038/ngeo2817

Reinen, L.A., Weeks, J.D., 1993. Determination of rock friction constitutive parameters using an iterative least-squares inversion method. *Journal of Geophysical Research: Solid Earth* 98(B9), 15937–15950. doi: 10.1029/93JB00780

Rogers, G., Dragert, H., 2003. Episodic tremor and slip on the Cascadia subduction zone: the chatter of silent slip. *Science* 300(5627), 1942–1943. doi: 10.1126/science.1084783

Ruina, A., 1983. Slip instability and state variable friction laws. *Journal of Geophysical Research: Solid Earth* 88(B12), 10359–10370. doi: 10.1029/JB088iB12p10359

Sacks, I.S., Suyehiro, S., Linde, A.T., Snoke, J.A., 1978. Slow earthquakes and stress redistribution. *Nature* 275(5681), 599–602.

Saffer, D.M., Frye, K.M., Marone, C., Mair, K., 2001. Laboratory results indicating complex and potentially unstable frictional behavior of smectite clay. *Geophysical Research Letters* 28(12), 2297–2300. doi: 10.1029/2001GL012869

Saffer, D.M., Lockner, D.A., McKiernan, A., 2012. Effects of smectite to illite transformation on the frictional strength and sliding stability of intact marine mudstones. Geophysical Research Letters 39(11). doi: 10.1029/2012GL051761

Saffer, D.M., Marone, C., 2003. Comparison of smectite- and illite-rich gouge frictional properties: application to the updip limit of the seismogenic zone along subduction megathrusts. *Earth and Planetary Science Letters* 215(1–2), 219–235. doi: 10.1016/S0012-821X(03)00424-2

Saffer, D.M., Tobin, H.J., 2011. Hydrogeology and Mechanics of Subduction Zone Forearcs: Fluid Flow and Pore Pressure. Annual Reviews of Earth Planetary Sciences 39, 157–186. doi: 10.1146/anurev-earth-040610-133408

Saffer, D.M., Wallace, L.M., 2015. The frictional, hydrologic, metamorphic and thermal habitat of shallow slow earthquakes. *Nature Geoscience* 8(8), 594–600. doi: 10.1038/ngeo2490

Saito, T., Ujiie, K., Tsutsumi, A., Kameda, J., Shibazaki, B., 2013. Geological and frictional aspects of very-low-frequency earthquakes in an accretionary prism. *Geophysical Research Letters* 40(4), 703–708. doi: 10.1002/grl.50175

Scholz, C.H., 1998. Earthquakes and friction laws. *Nature* 391(6662), 37–42. doi: 10.1038/34097

Scuderi, M.M., Marone, C., Tinti, E., Di Stefano, G., and Collettini, C., 2016. Precursory changes in seismic velocity for the spectrum of earthquake failure modes, *Nature Geoscience*, 9, 695–700, doi:10.1038/ngeo2775

Shibazaki, B., Iio, Y., 2003. On the physical mechanism of silent slip events along the deeper part of the seismogenic zone. *Geophysical Research Letters* 30(9). doi: 10.1029/2003GL017047

Shibazaki, B., Shimamoto, T., 2007. Modelling of short-interval silent slip events in deeper subduction interfaces considering the frictional properties at the unstable-stable transition regime. *Geophysical Journal International* 171(1), 191–205. doi: 10.1111/j.1365-246X.2007.03434.x

Shimamoto, T. and Logan, J.M., 1981. Effects of simulated clay gouges on the sliding behavior of Tennessee sandstone. *Tectonophysics* 75(3–4), 243–255. doi: 10.1016/0040-1951(81)90276-6

Tembe, S., Lockner, D.A., Wong, T-f., 2010. Effect of clay content and mineralogy on frictional sliding behavior of simulated gouges: Binary and ternary mixtures of quartz, illite, and montmorillonite. *Journal of Geophysical Research: Solid Earth* 115(B3). doi: 10.1029/2009JB006383

Tembe, S., Lockner, D., Wong, T-f., 2009. Constraints on the stress state of the San Andreas Fault with analysis based on core and cuttings from San Andreas Fault Observatory at Depth (SAFOD) drilling phases 1 and 2. *Journal of Geophysical Research* 114(B11). doi: 10.1029/2008JB005883

Tesei, T., Lacroix, B., Collettini, C., 2015. Fault strength in thin-skinned tectonic wedges across the smectite-illite transition: Constraints from friction experiments and critical tapers. *Geology* 43(10), 923–926. doi:10.1130/G36978.1

Tullis, T.E., Weeks, J.D., 1986. Constitutive Behavior and Stability of Frictional Sliding of Granite. *Pure and Applied Geophysics* 124(3), 383–414.

Ujiie, K., Tanaka, H., Saito, T., Tsutsumi, A., Mori, J.J., Kameda, J., Brodsky, E.E., Chester, F.M., Eguchi, N., Toczko, S., 2013. Low coseismic shear stress on the Tohoku-Oki megathrust determined from laboratory experiments. *Science* 342(6163), 1211–1214. doi: 10.1126/science.1243485

Underwood, M.B., 2002. Strike-parallel variations in clay minerals and fault vergence in the Cascadia subduction zone. *Geology* 30(2), 155–158. doi: 10.1130/0091-7613(2002)030<0155:SPVICM>2.0.CO;2

Underwood, M.B., 2007. Clay Mineral Composition and Diagenesis: Effects on the Location and Behavior of Faults in the Frontal Portions of Subduction Zones. *Scientific Drilling*, 61–63.

Vallée, M., Nocquet, J.M., Battaglia, J., Font, Y., Segovia, M., Régnier, M., Mothes, P., Jarrin, P., Cisneros, D., Vaca, S., Yepes, H., Martin, X., Béthoux, N., Chlieh, M., 2013. Intense interface seismicity triggered by a shallow slow slip event in the Central Ecuador subduction zone. J. Geophys. Res. Solid Earth 118(6), 2965–2981. doi: 10.1002/jgrb.50216

Vannucchi, P., Spagnuolo, E., Aretusini, S., Di Toro, G., Ujiie, K., Tsutsumi, A., Nielsen, S., 2017. Past seismic slip-to-the-trench recorded in Central America megathrust. *Nature Geoscience*, 10(12), 935. doi: 10.1038/s41561-017-0013-4

Verberne, B.A., De Bresser, J.H., Niemeijer, A.R., Spiers, C.J., De Winter, D.M., Plümper, O., 2013. Nanocrystalline slip zones in calcite fault gouge show intense crystallographic preferred orientation: Crystal plasticity at sub- seismic slip rates at 18–150 ˚C. *Geology* 41(8), 863–866. doi: 10.1130/G34279.1

Verberne, B.A., Plumper, O., Matthijs de Winter, D.A., Spiers, C.J., 2014a. Superplastic nanofibrous slip zones control seismogenic fault friction. *Science* 346(6215), 1342–1344. doi: 10.1126/science.1259003

Verberne, B.A., Spiers, C.J., Niemeijer, A.R., De Bresser, J.H.P., De Winter, D.A.M., Plümper, O., 2014b. Frictional Properties and Microstructure of Calcite-Rich Fault Gouges Sheared at Sub-Seismic Sliding Velocities. *Pure and Applied Geophysics* 171(10), 2617–2640. doi: 10.1007/s00024-013-0760-0

Vogt, C., Lauterjung, J., Fischer, R.X., 2002. Investigation of the clay fraction (<2 μm) of the clay minerals society reference clays. *Clays and Clay Minerals* 50(3), 388–400.

Wallace, L.M., Beavan, J., 2006. A large slow slip event on the central Hikurangi subduction interface beneath the Manawatu region, North Island, New Zealand. Geophysical Research Letters 33(11). doi: 10.1029/2006GL026009

Wallace, L.M., Beavan, J., 2010. Diverse slow slip behavior at the Hikurangi subduction margin, New Zealand. *Journal of Geophysical Research: Solid Earth* 115(B12). doi: 10.1029/2010JB007717

Wallace, L.M., Beavan, J., Bannister, S., Williams, C., 2012. Simultaneous long-term and short-term slow slip events at the Hikurangi subduction margin, New Zealand: Implications for processes that control slow slip event occurrence, duration, and migration. *Journal of Geophysical Research: Solid Earth* 117(B11). doi: 10.1029/2012JB009489

Wallace, L.M., Beavan, J., McCaffrey, R., Darby, D., 2004. Subduction zone coupling and tectonic block rotations in the North Island, New Zealand. *Journal of Geophysical Research: Solid Earth* 109(B12). doi: 10.1029/2004JB003241

Wallace, L.M., Kaneko, Y., Hreinsdóttir, S., Hamling, I., Peng, Z., Bartlow, N., D'Anastasio, E., Fry, B., 2017. Large-scale dynamic triggering of shallow slow slip enhanced by overlying sedimentary wedge. *Nature Geoscience* 10(10). doi: 10.1038/ngeo3021

Wallace, L.M., Reyners, M., Cochran, U., Bannister, S., Barnes, P.M., Berryman, K., Downes, G., Eberhart-Phillips, D., Fagereng, A., Ellis, S., Nicol, A., McCaffrey, R., Beavan, R.J., Henrys, S., Sutherland, R., Barker, D.H.N., Litchfield, N., Townend, J., Robinson, R., Bell, R., Wilson, K., Power, W., 2009. Characterizing the seismogenic zone of a major plate boundary subduction thrust: Hikurangi Margin, New Zealand. *Geochemistry, Geophysics, Geosystems* 10(10). doi: 10.1029/2009GC002610

Wallace, L.M., Webb, S.C., Ito, Y., Mochizuki, K., Hino, R., Henrys, S., Schwartz, S.Y., Sheehan, A.F., 2016. Slow slip near the trench at the Hikurangi subduction zone, New Zealand. *Science* 352(6286), 701–704. doi: 10.1126/science.aaf2349

Walter, J.I., Schwartz, S.Y., Protti, J.M., Gonzalez, V., 2011. Persistent tremor within the northern Costa Rica seismogenic zone. *Geophysical Research Letters* 38(1). doi: 10.1029/2010GL045586

Zhang, X., Spiers, C.J., 2005. Compaction of granular calcite by pressure solution at room temperature and effects of pore fluid chemistry. *International Journal of Rock Mechanics and Mining Sciences* 42(7–8), 950–960. doi: 10.1016/j.ijrmms.2005.05.01

Zhang, X., Spiers, C.J., Peach, C.J., 2010. Compaction creep of wet granular calcite by pressure solution at 28 ˚C to 150 ˚C. *Journal of Geophysical Research: Solid Earth* 115(B9). doi: 10.1029/2008JB005853

Table 1 Friction experiments conducted on sediment from ODP Site 1124C. Note that in biaxial and direct shear deformation experiments, normal stress is independently controlled while in triaxial deformation experiments, normal stress is a function of the controlled confining pressure and the measured axial stress. Depths were calculated using experimental effective stress values and assuming a pressure gradient of 25 MPa/km less the hydrostatic pressure of 10 MPa/km (giving an effective stress gradient of 15 MPa/km) and a geotherm of 10 ˚C/km. This assumes that effective stress is approximately equivalent to effective overburden on a shallowly dipping fault.

Experiment Number	Apparatus	Equivalent Depth (km)	σ_N (BRAVA, slow) (MPa)	P_c (BRAVA, triax) (MPa)	Pp (MPa)	σ_{eff} (MPa)	T_{set} (˚C)	T_{samp}, mean (˚C)	T_{samp}, std (˚C)	Velocity steps (µm/s)	Final shear strain*
i205	BRAVA	0.067	0.8	0.7	0.5	1	20	------	------	1-300	6.6
i206	BRAVA	0.33	4	2	1	5	20	------	------	1-300	10.4
i207	BRAVA	1.67	16	10	1	25	20	------	------	1-300	12.1
B628	Bremen Direct Shear	0.67	10	------	------	10	20	------	------	0.0017-0.0051	------
B718	Bremen Direct Shear	0.67	10	------	------	10	20	------	------	0.0017-0.51	------
B721	Bremen Direct Shear	0.67	10	------	------	10	20	------	------	0.17-51	------
T035	LDEO Triax	10	------	165	12	165.9	100	106.86	3.88	1.41-42.43	6.0
T036	LDEO Triax	7	------	115	10	125.5	70	73.5	3.52	1.41-42.43	6.1
T037	LDEO Triax	5	------	65	5	72.4	50	47.54	3.13	1.41-141	8.1
T039	LDEO Triax	------	------	165	15	159.8	20	------	------	1.41-141	6.6
T040	LDEO Triax	------	------	165	15	156.0	70	73.34	3.8	1.41-141	6.3
T041	LDEO Triax	------	------	115	10	104.3	20	------	------	1.41-141	9.1
T042	LDEO Triax	------	------	65	5	60.4	20	------	------	1.41-141	8.7
T044	LDEO Triax	5	------	65	5	68.0	50	48	3.36	1.41-141	7.3
T045	LDEO Triax	2	------	25	1	26.2	20	------	------	1.41-141	7.5

* Shear strains for BRAVA experiments are calculated using measured displacement normal to the gouge layer, while shear strains for triaxial deformation experiments are estimated using a shear thickness of 1 mm as discussed in the text. Strains for direct shear are not provided due to the fact that the thickness of the sliding layer is not quantified.

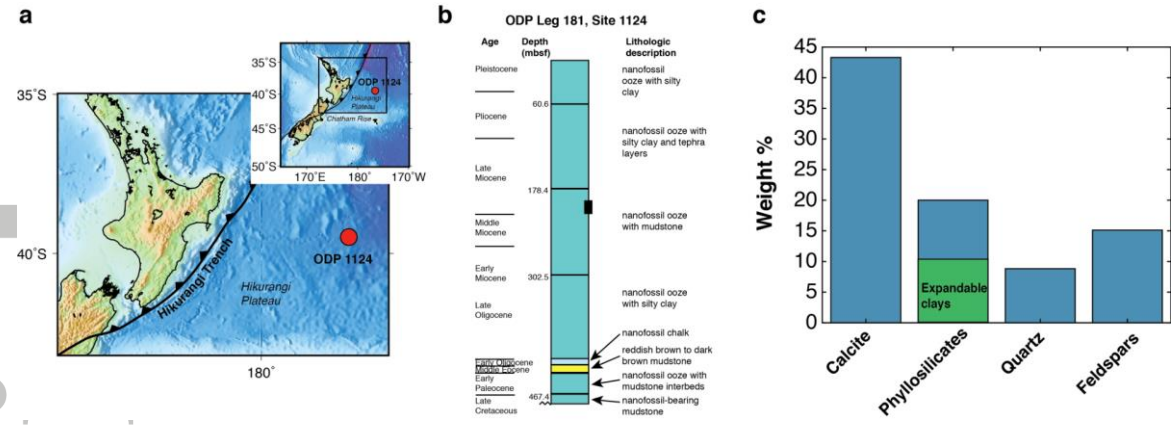

Figure 1. a) Map of New Zealand with location of the Hikurangi Trench just east of the North Island. Red dot shows the location of Site 1124 which drilled through the input sediments. The sediment used in this study comes from ODP Site 1124. Regional map of New Zealand is shown as an inset. b) Generalized stratigraphy of incoming sediments to the Hikurangi Trench from ODP Site 1124. Sample used in this study was taken between 194 and 213.48 mbsf, indicated by the black box on the right hand side of the stratigraphic column. c) XRD analysis shows the sediment is composed of 43.3% calcite, 20% phyllosilicates (~10% expandable clays shown in green), 9% quartz, and 15% feldspar.

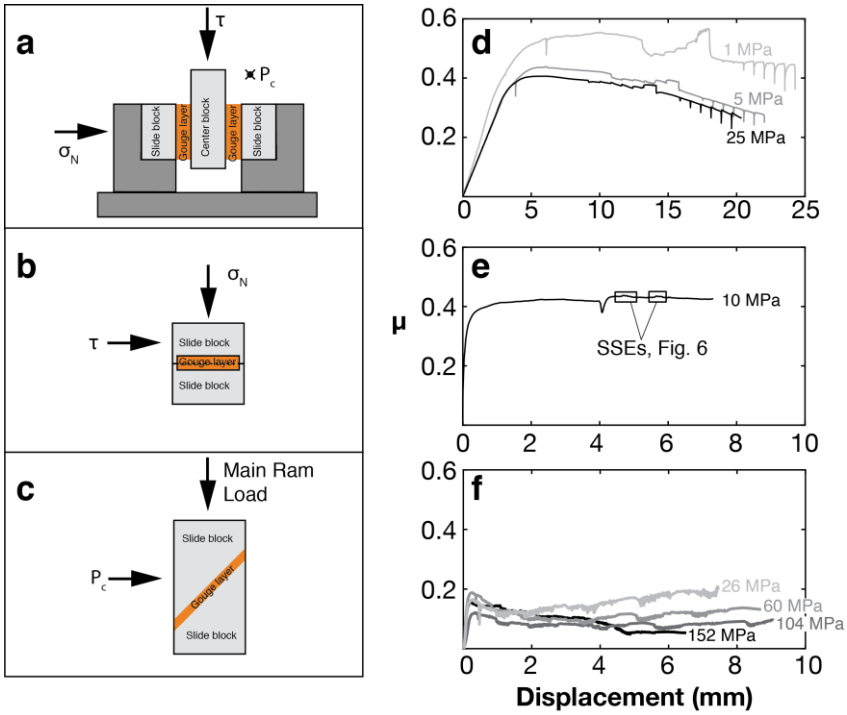

Figure 2. Sample configurations for the three apparatuses used in this study (a, b, c) as well as friction vs. displacement plotted for each apparatus (d, e, f). Friction curves are labeled with the experimental effective stress. In (f) only room temperature triaxial experiments are plotted for clarity. Effective stress values indicated for the triaxial experiments are mean effective stress during the experiment (Table S1). Note that the amount of displacement achieved in BRAVA is significantly greater than the other experiments.

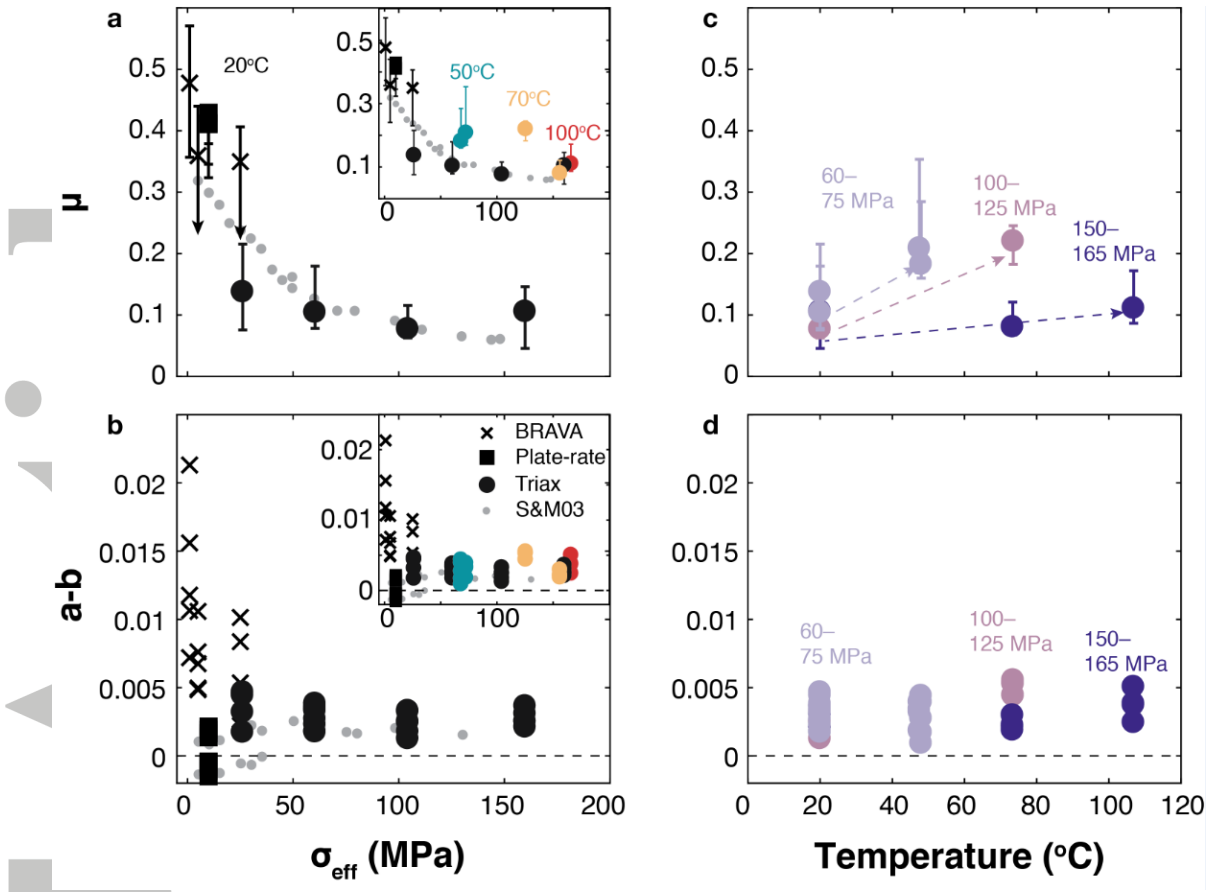

Figure 3. a) Friction (μ) and b) *a–b* plotted against effective stress (σ_{eff}) for room temperature experiments with insets also showing high temperature experiments in color as indicated. Different symbols represent experiments conducted on different apparatus (x's for BRAVA, squares for slow experiments, and circles for triax experiments). Symbols represent the median friction value with error bars showing the range of friction values observed (a) and the range of *a–b* values for all velocity steps in a given experiment (b). In (a) and (b), grey dots represent data from experiments on pure smectite from Saffer and Marone (2003). At room temperature, both friction and *a–b* decrease with increasing effective stress. c) Friction and d) *a–b* plotted against temperature for triaxial experiments, with color representing effective stress as indicated. Note a slight positive correlation between both μ and *a–b* and temperature.

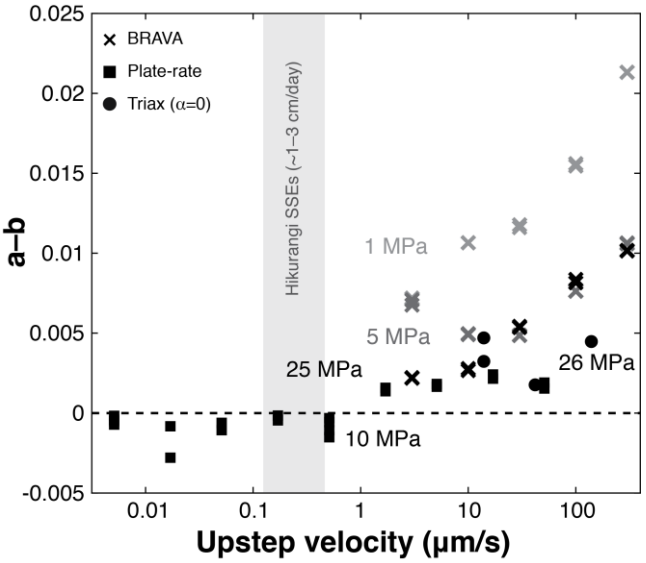

Figure 4. Velocity-dependence as a function of up-step velocity. Effective stress as indicated. A clear trend towards increasing *a–b* values with higher sliding velocity is seen in the lowest effective stress experiments (BRAVA). The lowest *a–b* values are seen in the plate-rate experiment, conducted at 10 MPa. The approximate range in sliding velocities (Saffer and Wallace, 2015; Wallace and Beavan, 2010) at the northern Hikurangi subduction zone is indicated by the grey bar.

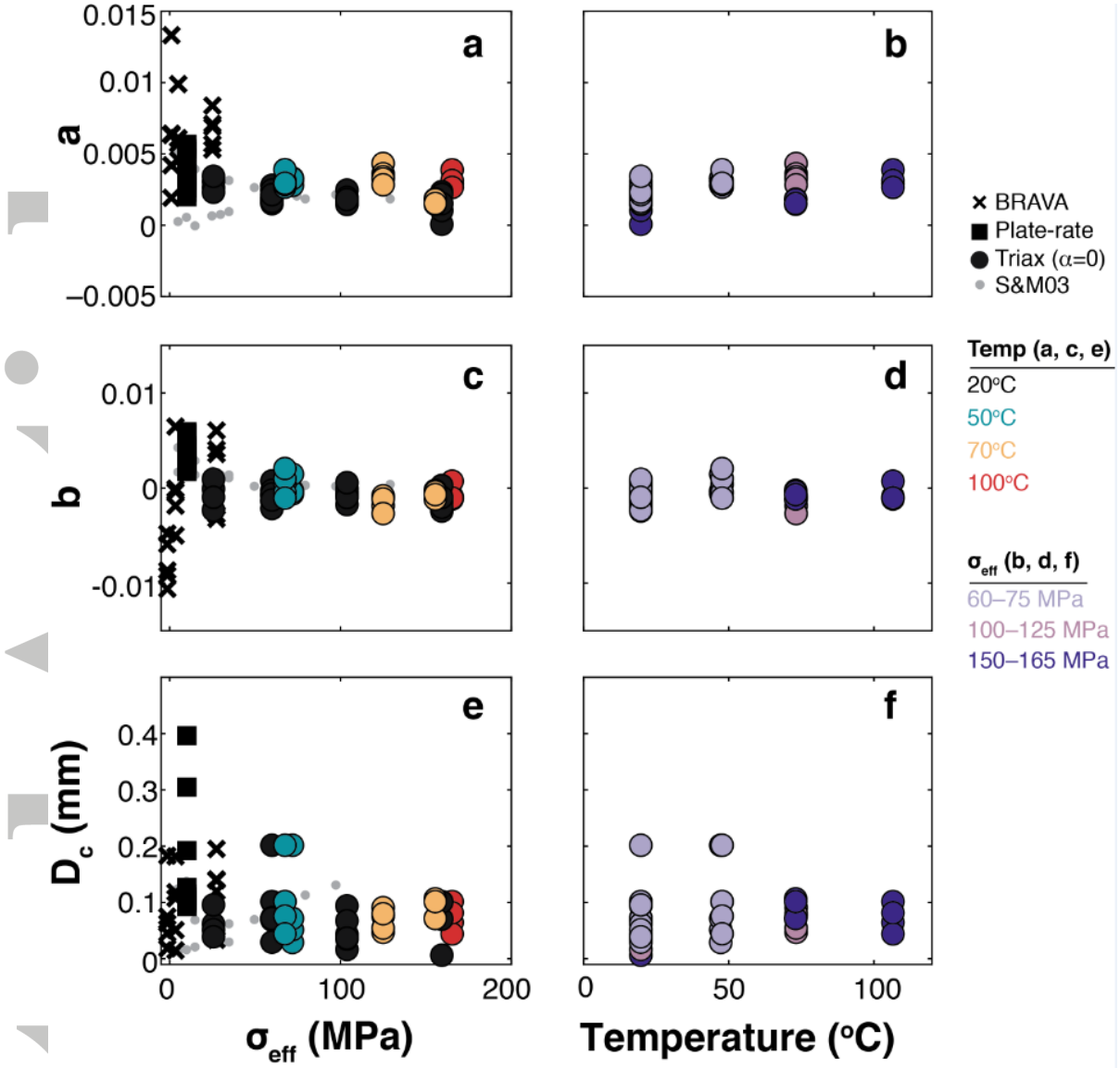

Figure 5. Rate-and-state friction parameters as a function of effective stress (a, c, and e) and temperature (b, d, and f). a) *a* values decrease with increasing effective stress and b) show a slight increase with increasing temperature. c) *b* values are more variable in the low stress experiments with values hovering around 0 for the high effective stress experiments and d) no clear trend as a function of temperature. e) D_c values show no significant trend with effective stress or f) temperature. c) Plotted *b* values in the BRAVA and plate-rate experiments represent b_1+b_2. e) D_c in the BRAVA and plate-rate experiments, black symbols represent $D_{c1}+D_{c2}$. In a), c), and e), grey dots represent data from experiments on pure smectite from Saffer and Marone (2003).

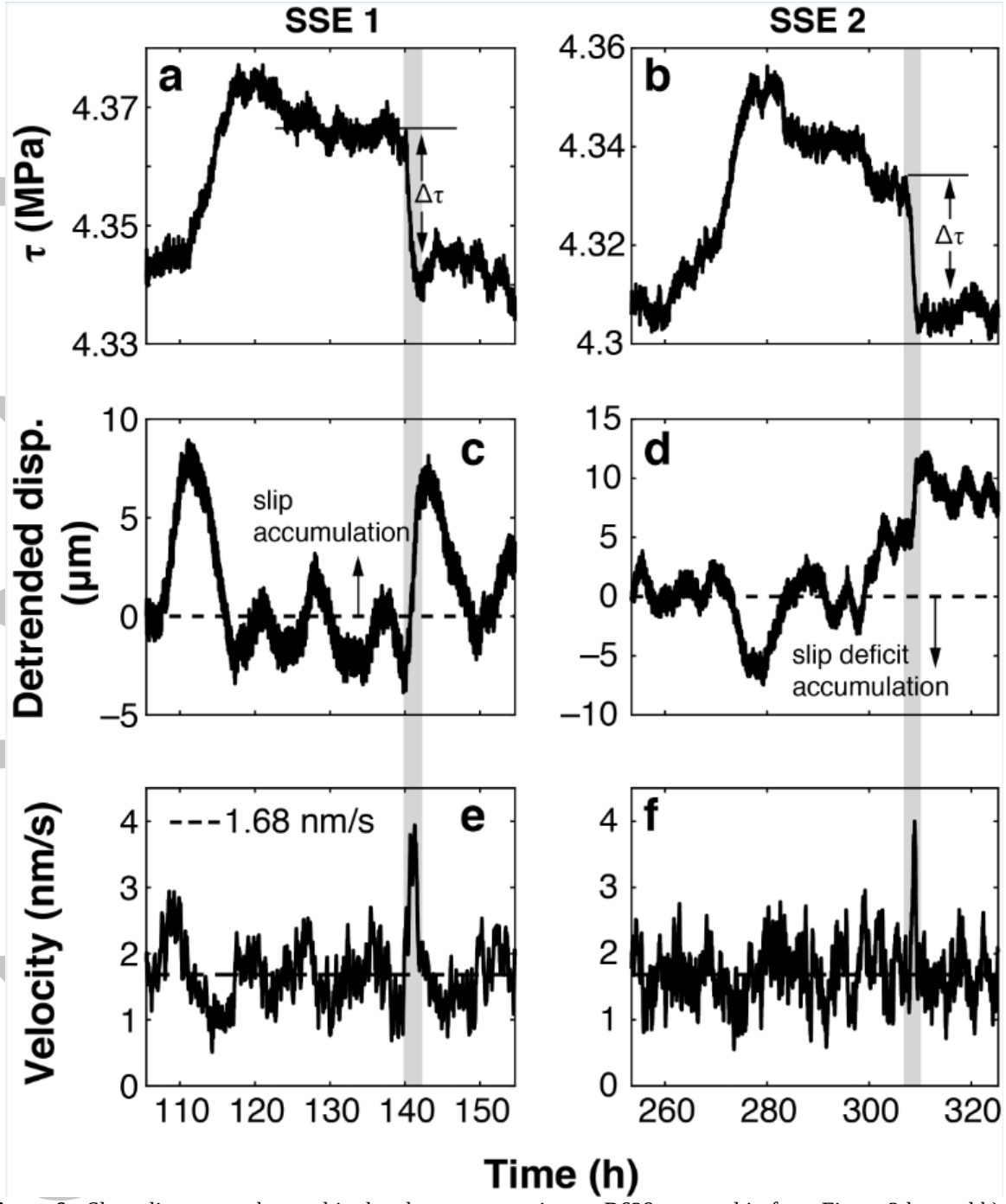

Figure 6. Slow slip events observed in the plate-rate experiment, B628, zoomed in from Figure 2d. a and b) In both SSEs, shear stress drops by ~0.03 Pa. c) Displacement in SSE 1 shows a decrease in slip accumulation at the beginning and an increase in slip accumulation at the end of the slip event. d) In SSE 2, a slip deficit is accumulated during the initial shear stress accumulation. e and f) During both SSEs, a peak in slip velocity is observed at the time of final stress drop.

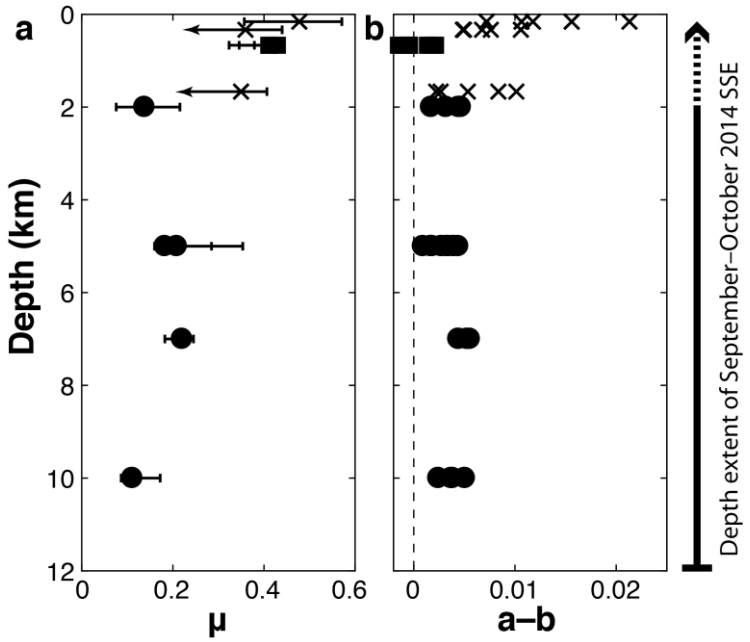

Figure 7. Frictional strength and stability with depth. a) Friction and b) velocity-dependence for samples conducted at effective stress and temperature conditions expected for a given depth in the Hikurangi subduction zone are plotted against depth. We see a reduction in friction coefficient and in *a–b* with increasing depth for traditional velocity-stepping experiments. The depth extent of the September–October 2014 SSE in Hikurangi determined by Wallace et al (2016) is shown to the right. The dotted line represents the possible extension of this SSE to the trench, though instrumental constraints prevented them from resolving this shallowest extent.